Geophysical Research Letters

RESEARCH LETTER
10.1029/2018GL081401

Special Section:
Cassini's Final Year: Science Highlights and Discoveries

Seasonal Evolution of Titan's Stratosphere During the Cassini Mission

N. A. Teanby[1], M. Sylvestre[1], J. Sharkey[1], C. A. Nixon[2], S. Vinatier[3], and P. G. J. Irwin[4]

[1]School of Earth Sciences, University of Bristol, Bristol, UK, [2]Planetary Systems Laboratory, NASA Goddard Space Flight Center, Greenbelt, MD, USA, [3]LESIA, Observatoire de Paris, Université PSL, CNRS, Sorbonne Université, Université Paris Diderot, Sorbonne Paris Cité, Meudon, France, [4]Atmospheric, Oceanic and Planetary Physics, Department of Physics, and Clarendon Laboratory, University of Oxford, Oxford, UK

Abstract Titan's stratosphere exhibits significant seasonal changes, including breakup and formation of polar vortices. Here we present the first analysis of midinfrared mapping observations from Cassini's Composite InfraRed Spectrometer to cover the entire mission (L_s=293–93°, 2004–2017)—midnorthern winter to northern summer solstice. The north polar winter vortex persisted well after equinox, starting breakup around $L_s \sim 60°$ and fully dissipating by $L_s \sim 90°$. Absence of enriched polar air spreading to lower latitudes suggests large-scale circulation changes and photochemistry control chemical evolution during vortex breakup. South polar vortex formation commenced soon after equinox and by $L_s \sim 60°$ was more enriched in trace gases than the northern middle-winter vortex and had temperatures ~20 K colder. This suggests that early-winter and middle-winter vortices are dominated by different processes—radiative cooling and subsidence-induced adiabatic heating respectively. By the end of the mission (L_s=93°) south polar conditions were approaching those observed in the north at L_s=293°, implying seasonal symmetry in Titan's vortices.

Plain Language Summary The Cassini spacecraft observed Saturn's largest moon, Titan, during its 13-year tour of the Saturn system. This allowed temperature and gas composition to be measured for almost half a Titan year, which lasts 29.46 Earth years. Spectra measured by Cassini's infrared spectrometer show that Titan's winter poles are much colder and significantly more enriched in trace gas species than more equatorial latitudes. These observations can be explained by the presence of winter polar vortices, where sinking air enriches the composition of the lower atmosphere and isolation by strong vortex winds allows enhanced cooling in the winter darkness. The coldest temperatures and most extreme trace gas concentrations were seen at Titan's southern pole during early winter and vortex formation.

Key Points:
- Early- and middle-winter polar vortices have distinct behaviors and different dominant processes
- Large-scale dynamics and photochemistry determine polar chemical evolution during vortex breakup
- The northern winter vortex persisted until late spring, with breakup completed by midsummer

Supporting Information:
- Supporting Information S1
- Data Set S1
- Data Set S2
- Data Set S3
- Table S1

Correspondence to:
N. A. Teanby,
n.teanby@bristol.ac.uk

Citation:
Teanby, N. A., Sylvestre, M., Sharkey, J., Nixon, C. A., Vinatier, S., & Irwin, P. G. J. (2019). Seasonal evolution of Titan's stratosphere during the Cassini mission. *Geophysical Research Letters*, *46*, 3079–3089. https://doi.org/10.1029/2018GL081401

Received 20 NOV 2018
Accepted 19 FEB 2019
Accepted article online 25 FEB 2019
Published online 18 MAR 2019

1. Introduction

Saturn's largest moon Titan has a thick atmosphere comprising ~98% nitrogen and ~2% methane with ~1.5 bar surface pressure (Fulchignoni et al., 2005). Titan has a rich C-N-H photochemistry originating from radicals formed by dissociation of N_2 and CH_4 by ultraviolet photons and magnetospheric electrons (Dobrijevic et al., 2014; Krasnopolsky, 2009; Lavvas et al., 2008; Loison et al., 2015; Vuitton et al., 2019; Wilson & Atreya, 2004). These radicals produce a wide range of higher-order hydrocarbon and nitrile trace gas species with lifetimes ranging from a few seconds to thousands of years (Vuitton et al., 2019; Wilson & Atreya, 2004). Oxygen species also contribute to atmospheric chemistry (Dobrijevic et al., 2014; Hörst et al., 2008), but only H_2O, CO, and CO_2 have been detected so far. Trace gases are produced in the upper atmosphere (~1,000 km) and condense in the cold lower stratosphere, giving rise to vertical abundance profiles that have increasing volume mixing ratio (VMR) with increasing altitude (Coustenis et al., 1991; Teanby et al., 2007; Vinatier et al., 2007). The vertical mixing timescale between source and sink regions controls the vertical gradient, with the shortest-lifetime gases having the steepest vertical gradients due to their more rapid loss away from the source region (Teanby et al., 2009).

Here we use observations of trace gas emission features taken by the Cassini spacecraft's Composite InfraRed Spectrometer (CIRS) (Flasar et al., 2004) to determine how Titan's atmosphere changes with the seasons. These observations can be used to determine Titan's atmospheric temperature and composition, inform and constrain photochemical models, and probe Titan's atmospheric circulation (Bézard, 2014; Teanby,

de Kok, et al., 2008). Cassini completed 294 Saturn orbits and 127 close Titan flybys between orbital insertion on 1 July 2004 (L_s=293°) and its final plunge into Saturn's atmosphere on 15 September 2017 (L_s=93°). Saturn/Titan's year lasts 29.46 Earth years, so Cassini's 13-year Saturn system tour covered almost half a Saturn/Titan year. Saturn's, and hence Titan's, obliquity is 26.7°, so significant seasonal effects were observed during the mission, spanning northern winter to northern summer solstice. Terrestrial general circulation models (GCMs) adapted to Titan's atmosphere predict that middle atmosphere (stratosphere and mesosphere) meridional circulation is dominated by a single south-to-north circulation cell during northern winter, with upwelling in the southern hemisphere and subsidence at the north pole. This circulation reverses around equinox via a short-lived intermediate circulation with two hemispheric cells that upwell at the equator and subside at both poles (Hourdin et al., 1995; Lebonnois et al., 2012, 2014; Lora et al., 2015; Newman et al., 2011). Such changes have been investigated by observing how short- and intermediate-lifetime trace gas distributions vary over the mission. For example, subsidence advects photochemical species downward, which causes stratospheric abundances to increase. Therefore, gas abundance can be used as a tracer of vertical motion (Teanby et al., 2012). This is particularly obvious over Titan's winter poles, where subsidence can lead to very large trace gas enrichments (Coustenis et al., 2016, 2018; Teanby, de Kok, et al., 2008; Teanby et al., 2012, 2017; Vinatier et al., 2010, 2015).

Cassini's varied orbital tour provided a unique vantage point for observing Titan's winter pole, which has been known since the Voyager flybys to be the most enriched in trace gases (Coustenis & Bézard, 1995). Cassini observations are particularly valuable as observing the winter pole is not possible from Earth due to viewing geometry. Subsets of the Cassini data have been analyzed previously and show that in northern winter the north pole was much more enriched in trace gases than other latitudes (Coustenis et al., 2007, 2010, 2016; Flasar et al., 2005; Sylvestre et al., 2018; Teanby et al., 2006, 2010b; Teanby, Irwin, et al., 2008; Vinatier et al., 2010). Thermal winds derived from stratospheric temperature fields show that the northern winter pole was surrounded by a strong polar vortex, which isolated the polar air mass, allowing extreme gas enrichments to develop (Achterberg et al., 2008, 2011; Teanby, de Kok, et al., 2008; Teanby et al., 2010b). However, there is also some evidence for cross-vortex mixing of intermediate-lifetime species such as HCN in the middle stratosphere (Teanby, de Kok, et al., 2008). Short-lifetime gases are more enriched due to their steeper vertical gradient and resulting greater sensitivity to downward advection (Teanby et al., 2009, 2010a).

Later in the mission, after the 2009 northern spring equinox, the south pole began to become enriched in trace gases, indicating that the circulation had reversed and subsidence was now occurring at the southern pole (Teanby et al., 2012). There was also compositional evidence for the transitional two-cell circulation predicted by numerical models (Vinatier et al., 2015). Following equinox, enrichment at the south pole was greater than that observed in the north at the start of the mission (Coustenis et al., 2018; Teanby et al., 2017). The south polar stratosphere also achieved extremely cold temperatures, which created ice clouds of HCN (de Kok et al., 2014) and benzene (Vinatier et al., 2018) at ~300 km. These cold temperatures were not observed in the north and could be caused by extreme trace gas enrichments acting as infrared coolers, combined with slow initial subsidence producing only modest levels of adiabatic heating (Teanby et al., 2017). This illustrates the importance of trace gases in Titan's overall atmospheric energy budget (Bézard et al., 1995, 2018; Teanby et al., 2017).

The meridional circulation also affects Titan's aerosols. Cassini's Visual and Infrared Mapping Spectrometer observations show winter subsidence is associated with thick lower stratosphere condensate clouds over the poles (Le Mouélic et al., 2018). Cassini's Imaging Science Subsystem observations of Titan's detached haze layer at 350–500 km imply upwelling speeds greater than haze particle free-fall velocity are required to dynamically clear the lower mesosphere of haze (West et al., 2018). These Visual and Infrared Mapping Spectrometer and Imaging Science Subsystem observations further confirm the meridional circulation inferred from Cassini CIRS and GCMs.

Here we present the first analysis of all CIRS midinfrared mapping sequences from the entire Cassini mission, spanning 2004–2017 (L_s = 293–93°, ΔL_s = 160°), almost half a Titan year. This unique data set allows stratospheric temperature and composition to be determined along with seasonal variations. Previous CIRS studies have been limited to southern latitudes only (e.g., Teanby et al., 2017) or only included data taken up until 2016 (e.g., Coustenis et al., 2018). In addition, our analysis uses an improved methodology, incorporating limb observation-based temperature a priori, which gives more robust temperature and composition

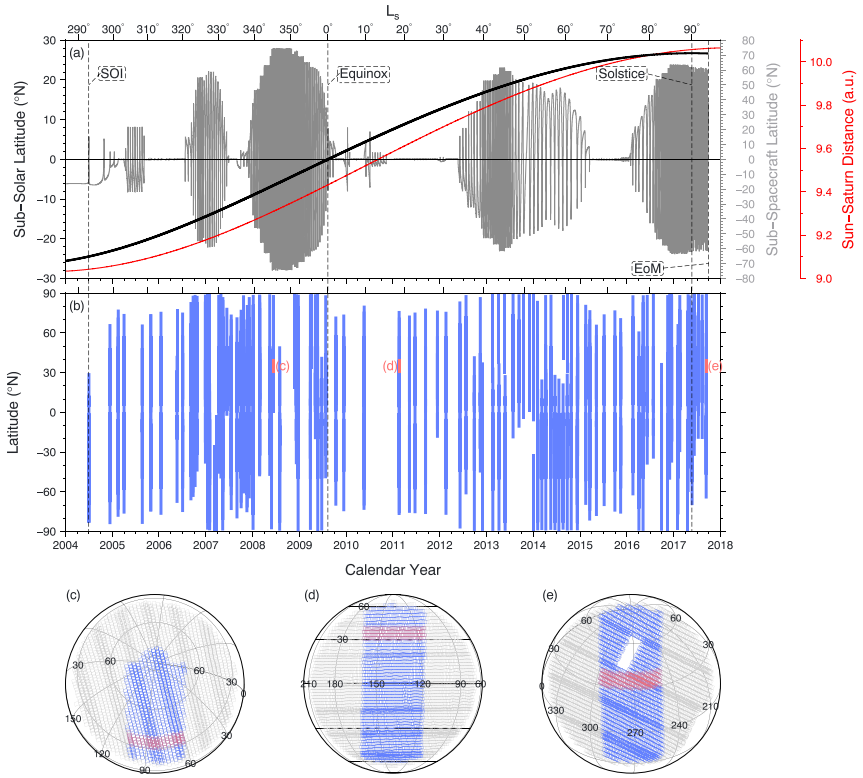

Figure 1. Cassini's Composite InfraRed Spectrometer data summary for the entire Cassini mission. (a) Evolution of subsolar latitude (black), subspacecraft latitude projected onto Saturn (gray), and Sun-Saturn distance throughout the mission (red). Saturn orbit insertion (SOI) until the end of mission (EoM) covers northern winter, northern spring equinox, and northern summer solstice. The complex tour includes four high orbital inclination periods, which give coverage of the north and south poles. (b) Latitude-time coverage of the 2.5-cm^{-1} resolution Cassini's Composite InfraRed Spectrometer nadir mapping observations. There are several data gaps at the poles, but overall, the CIRS data set has excellent coverage. (c–e) Examples of observation binning to improve signal-to-noise ratio. Gray shows the footprint of all spectra in an observation sequence, blue shows spectra which satisfy emission angle and geometry constraints, and red shows examples of spectra included in a 10° latitude bin (30–40°N). Example bin locations are indicated in (b).

inversions. CIRS has the advantage of high spatial and temporal resolution, including the polar regions, from a single instrument, which we take full advantage of by simultaneously analyzing the entire data set with the same methodology. Previous studies have only analyzed partial data sets, which made direct comparison between seasons more difficult. We use our analysis to answer three key questions: (1) are thermal and chemical behaviors of Titan's north and south polar vortices comparable? (2) what are the main factors controlling chemistry during polar vortex breakup? (3) how long does the winter polar vortex breakup take? These questions are essential for understanding Titan's atmospheric chemistry and dynamics, in addition to constraining future GCMs and photochemical models.

2. Radiative Transfer Analysis

CIRS observation coverage and example spatial binning to improve signal-to-noise ratio are shown in Figure 1. Observations sequences and data preprocessing are summarized in supporting information Table S1 and Text S1.

The inversion method is explained in detail in previous papers (Irwin et al., 2008; Teanby et al., 2006, 2010b; Teanby, Irwin, et al., 2008) and is briefly summarized here. Spectra were inverted for temperature and composition using the NEMESIS retrieval code (Irwin et al., 2008), which employs an optimal estimation technique. Partial derivatives of the forward modeled radiances were calculated analytically with respect to each model variable using radiative transfer theory. The temperature and composition were then iteratively adjusted to fit the data while remaining as close to the a priori profiles as possible (Irwin et al., 2008).

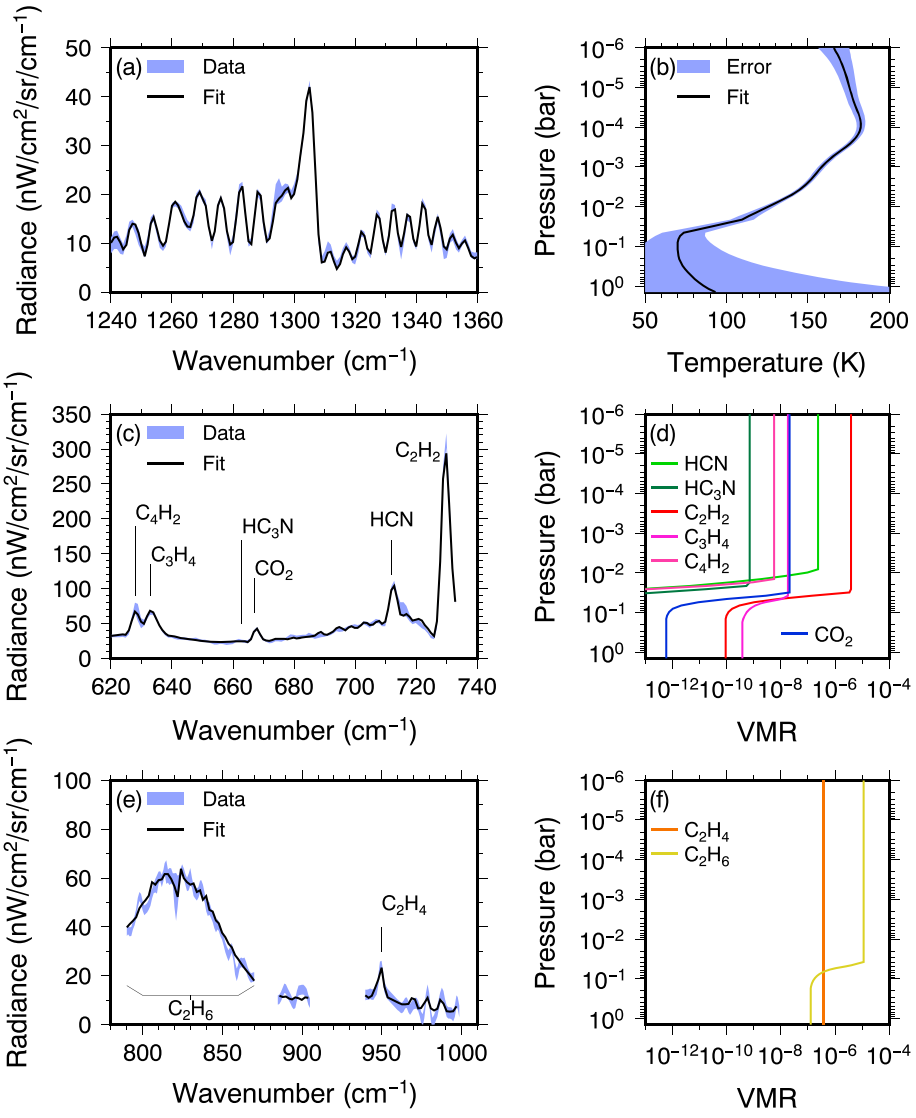

Figure 2. Example fits to Cassini's Composite InfraRed Spectrometer spectra at 75°N from Cassini's final Titan flyby (orbit 293). (a) Fit to the ν_4 CH_4 band in FP4 and (b) retrieved temperature profile used for the fit. (c, e) Fits to the trace gas vibrational features in the FP3 spectrum and (d, f) corresponding trace gas volume mixing ratio (VMR) profiles. All gases are assumed to have a uniform abundance profile above the condensation level. This simplified parameterization is sufficient to fit these data. Note that C_2H_4 does not condense under Titan's atmospheric conditions.

Here we use a two-stage inversion process similar to that in Teanby et al. (2010b). First, a continuous temperature profile was retrieved for each binned spectrum using the ν_4 methane band in FP4 over the spectral range 1,240–1,360 cm^{-1}. A latitude- and time-dependent temperature a priori (supporting information Text S2) was used as the starting point, with an a priori error σ varying as a function of latitude θ between σ_{eq} = 2 K at the equator and σ_{pole} = 5 K at the poles according to $\sigma = \sigma_{pole} - (\sigma_{pole} - \sigma_{eq})\cos\theta$. This accounted for the greater uncertainty in polar temperatures compared to the more stable and well-constrained equator, where we have the advantage of Huygens probe direct temperature measurements (Fulchignoni et al., 2005). A correlation length of 1.5 atmospheric scale heights was assumed for the off-diagonal elements of the temperature a priori covariance matrix to ensure a smooth temperature profile was retrieved (Irwin et al., 2008). Second, the temperature was fixed and uniform a priori gas profiles (supporting information Text S3) were scaled to provide the best fit to the observed spectra. Example fits to the data are shown in Figure 2 along with the corresponding fitted temperature and composition profiles.

Nadir observation sensitivity is limited to midstratosphere to lower mesosphere (~5–0.1 mbar), with peak information content at ~1 mbar. Near the winter pole the range of sensitivity is 1–0.01 mbar for cases with a

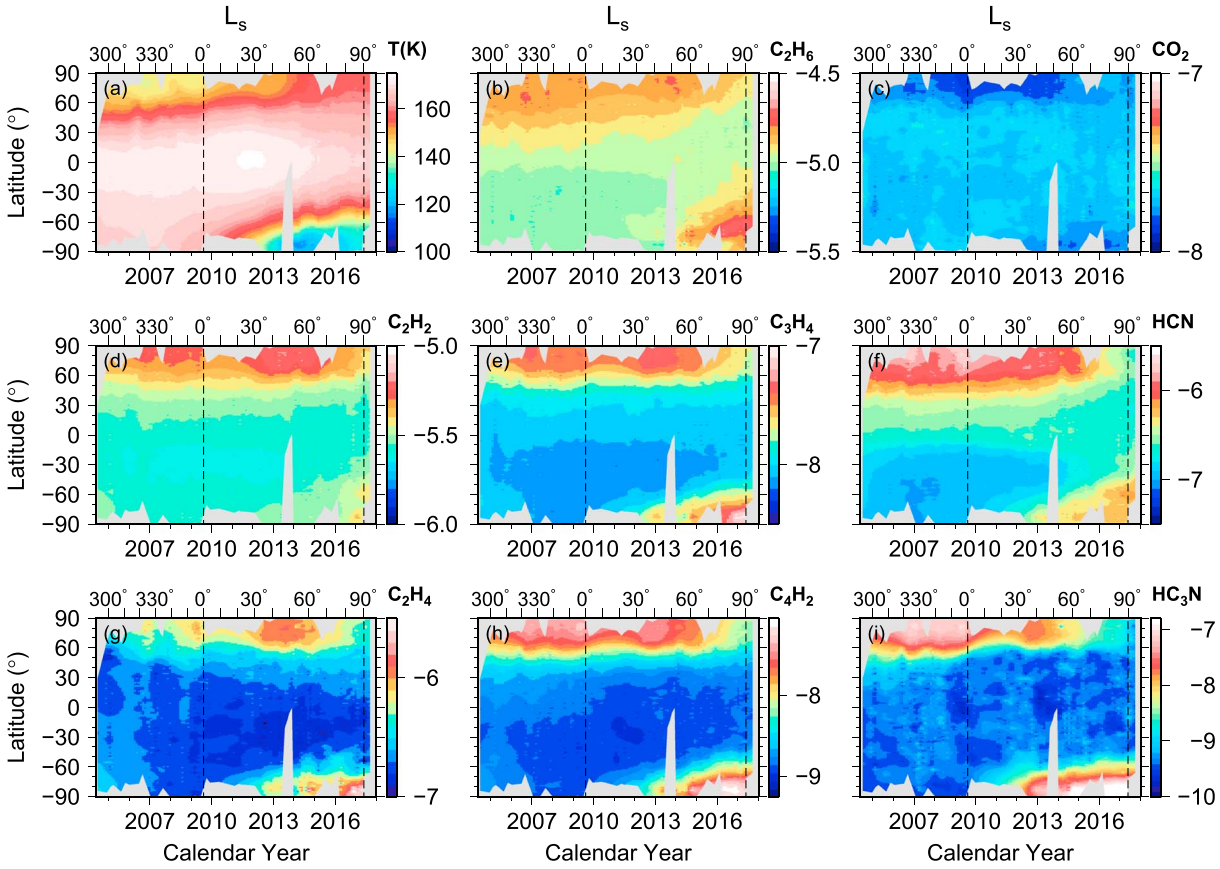

Figure 3. (a–i) Temperature and composition seasonal latitude variation at the 1-mbar pressure level. Temperature shows a warm equator and cold winter poles, with the south winter pole reaching the coldest temperatures. Composition variations show trace gas enrichment at the winter poles, again with the most extreme enrichment at the southern winter pole. Short-lifetime gases (C_4H_2 and HC_3N) have the largest enrichment, whereas the longest-lifetime gas (CO_2) does not vary significantly. North polar enrichment persists for ~60–90° of L_s after equinox. Vertical dashed lines show the 2009 northern spring equinox (L_s=0°) and 2017 northern summer solstice (L_s = 90°). The 1-mbar surfaces are fitted to irregularly spaced inversion results using a 2-D spline in tension (Smith & Wessel, 1990) with a grid spacing of 0.1 years (~1° of L_s) and 1° latitude. Gray areas indicate data gaps. Units of composition are $\log_{10}$(VMR).

hot stratopause and very cold lower to middle stratosphere. Contribution functions for both these cases are plotted in Teanby, Irwin, et al. (2008, their Figure 3).

3. Results

Figure 3 shows the latitudinal variation of temperature and composition at the 1-mbar pressure level with season for the entire Cassini mission. Figure 4 shows the seasonal variation in time series form for latitudes 80°S, 50°S, 0°N, 50°N, and 80°N. In this section we briefly discuss gross features of the temperature and composition results. Implications for Titan's atmosphere are considered in section 4.

3.1. Seasonal Temperature Variations

The midstratosphere 1-mbar temperatures shown in Figure 3 are warmest at the equator, with peak temperatures occurring at $L_s \sim 30°$. The equatorial temperature maximum moves northward as the season progresses from northern winter to northern summer, from ~10°S at L_s = 293° to ~0°N from $L_s \sim 30°$ onward. Equatorial temperatures at 1 mbar are relatively stable until $L_s \sim 30°$, after which they reduce by ~5 K between L_s = 30° and 93°. Temperatures at 1 mbar are coldest over the winter poles. The south pole has the coldest observed temperatures at this pressure level, occurring at $L_s \sim 60°$ in early southern winter.

Figure 4 shows the temperature variation at 5, 1, and 0.1 mbar for comparison. The temperature at 0.1 mbar displays the most seasonal variation, especially near the poles with a ~20 K preequinox cooling at the north pole and a ~45 K postequinox cooling and subsequent recovery at the south pole. The 5-mbar temperature exhibits a steady postequinox decrease for the equator and southern hemisphere and a steady increase in the northern hemisphere.

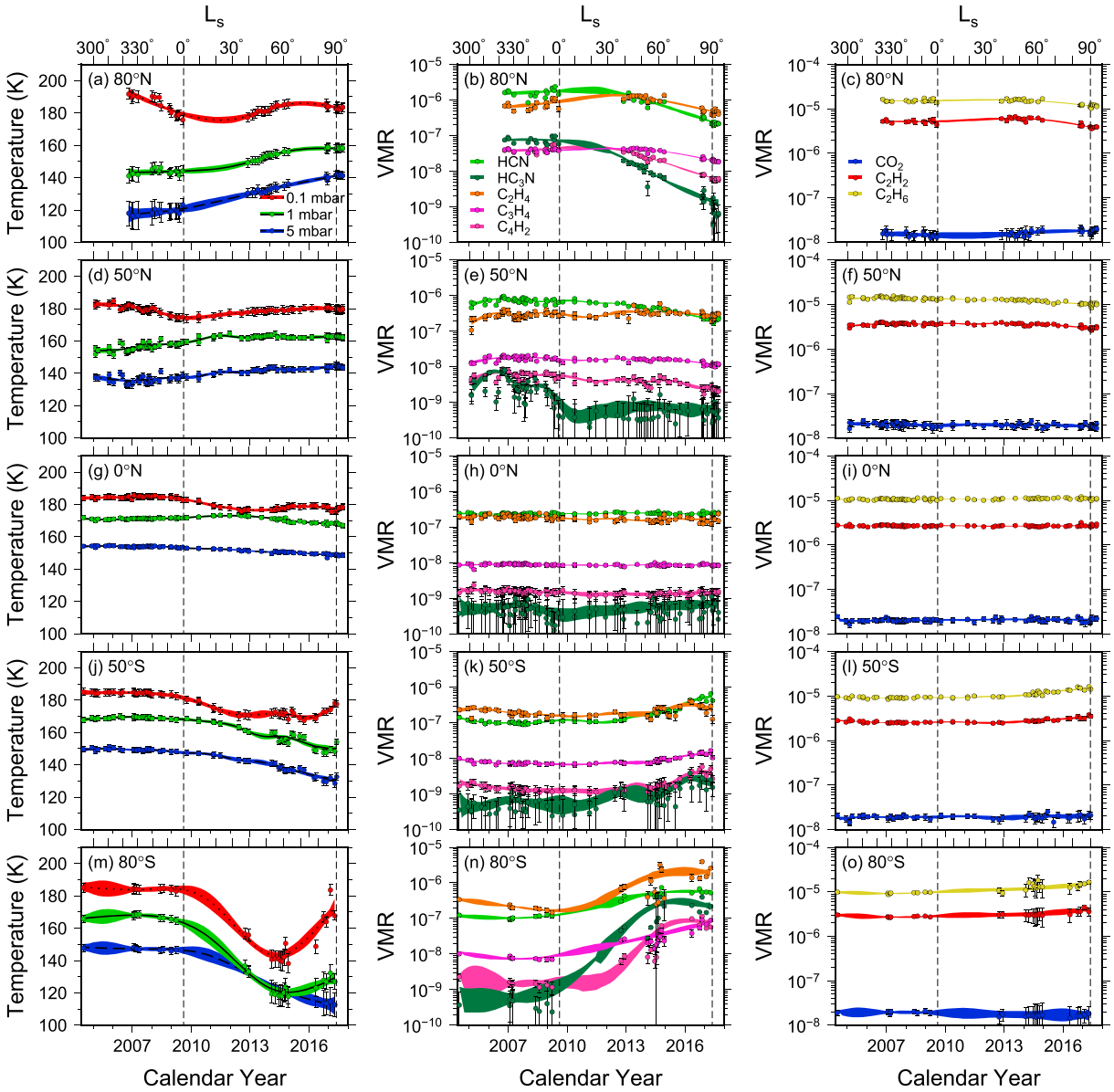

Figure 4. (a–o) Seasonal variation of temperature and composition at five latitudes. Temperature is shown at 5, 1, and 0.1 mbar. The 0.1-mbar pressure level is near the stratopause and is most sensitive to seasonal changes; for example, cooling of the stratopause hot spot preceding equinox and adiabatic heating from $L_s \sim 60°$ onward. Vertical dashed lines show the 2009 northern spring equinox and 2017 northern summer solstice. Points with errors are individual measurements, and lines with error envelopes are cubic b-spline fits under tension using a knot spacing of 15° of L_s for 0 and ±50°N, or 30° of L_s for ±80°N where data coverage is sparser (Teanby, 2007). VMR = volume mixing ratio.

3.2. Seasonal Composition Variations

Seasonal composition variations in Figure 3 are most appropriate for the 1-mbar level, based on contribution functions for the uniform profiles assumed here. Gases display a consistent behavior, with high concentrations over the poles during winter and approximately constant abundance at the equator, except for CO_2, which is roughly constant at all latitudes. The degree of enrichment over the poles depends on the gas species; HC_3N and C_4H_2 show the most extreme polar enrichments (2–3 orders of magnitude), whereas HCN, C_2H_2, C_2H_4, C_2H_6, and C_3H_4 have more modest enrichments (~1 order of magnitude or less). HC_3N and C_4H_2 react faster to the seasons than the more modestly enriched species, with HC_3N changing the fastest.

Note that absolute VMR values depend on profile assumptions, which can vary with latitude and season. For most gases, which have modest vertical gradients, this effect is small and the absolute VMRs can be

considered representative of the stratosphere. However, for short-lifetime gases like HC_3N and C_4H_2 that have very steep vertical gradients, the peak of the contribution function can shift to lower pressures, which leads to an overestimate of the stratospheric abundances (Teanby et al., 2006). Therefore, the uniform profile results presented here should only be used to inspect relative abundance variations as these are robust to profile assumptions. For example, relative abundance comparisons of HC_3N for different latitudes and times are valid, but absolute abundance comparisons between HC_3N and C_2H_2 are not valid. This is a fundamental limitation of the CIRS nadir spectra, which are sensitive to a broad pressure range and contain limited vertical information. Where absolute abundances are critical (e.g., for photochemical model profile comparisons) limb viewing data is required (e.g., Teanby et al., 2012; Vinatier et al., 2015).

4. Discussion

4.1. Polar Vortex General Characteristics

In general, Titan's stratospheric winter polar vortices are characterized by cold temperatures at 1 mbar, 20–50 K colder than at the equator (Figure 3). These cold temperatures cause a strong thermal gradient, which drives strong circumpolar winds, creates a potential vorticity gradient and mixing barrier, and effectively isolates the polar airmass from more equatorial latitudes (Achterberg et al., 2008, 2011; Flasar et al., 2005; Teanby, de Kok, et al., 2008). This allows subsiding air masses to enrich the polar stratosphere in trace gas species, which are advected down from the upper atmosphere photochemical production zone where they are more abundant (Teanby et al., 2009). Subsidence causes significant adiabatic heating at low pressures and leads to a hot stratopause over the winter pole (Achterberg et al., 2008; Teanby et al., 2017). Trace gas enrichment is largest for short-lifetime gases (HC_3N and C_4H_2), which tend to have steeper vertical gradients and are more susceptible to enrichment by subsidence (Teanby et al., 2009). The polar isolation is also most effective for short-lifetime species, whereas intermediate-lifetime species such as HCN and C_2H_2 can be mixed across the vortex barrier and leach to lower latitudes (Teanby, de Kok, et al., 2008). Longer-lifetime species are less enriched, with the very long lifetime species CO_2 showing virtually no variation, indicating a more uniform vertical profile consistent with a lifetime much longer than any dynamical timescale. This general picture is confirmed by our new results (Figures 3 and 4), but our longer time series covering the whole Cassini mission (L_s = 293–93°) allows further insight into vortex breakup and formation processes by observing both north and south poles (sections 4.2 and 4.3).

4.2. North Polar Vortex Evolution

The northern winter vortex was already well established when Cassini arrived at $L_s = 293°$ and extended from the north pole down to ~45°N. Initially, the 1-mbar temperatures were around 140 K, compared to 170 K at the equator, but had warmed to 160 K by the end of the mission at $L_s = 93°$ (Figure 4). As the mission progressed the vortex shrank in extent, being limited to latitudes north of 60°N from $L_s = 20°$ onward (Figure 3). Our results show the north polar vortex endured well beyond the northern spring equinox ($L_s = 0°$), maintaining cold temperatures and enriched trace gas abundances until at least late spring ($L_s \sim 60°$). After this point vortex dissipation was first visible in temperature and short-lifetime gases (HC_3N and C_4H_2) as a warming and abundance reduction. Early stages of vortex breakup were also visible in a subset of observations taken at 70°N before mid-2016 ($L_s < 80°$) by Coustenis et al. (2018).

The hot stratopause at 0.1 mbar driven by adiabatic heating was already cooling at $L_s \sim 320°$ and had stabilized in temperature by $L_s = 0°$, indicating a weakening in north polar subsidence. The midstratosphere at 1 mbar was slower to respond because of the longer radiative time constant, with temperatures increasing more gradually by ~20 K between $L_s = 0°$ and 90°, due to increased insolation. These observations indicate weakening of the vortex. A reduction in HC_3N and C_4H_2 abundance starting at $L_s \sim 50°$ is the first sign of vortex breakup. Longer-lifetime species dissipated over the proceeding L_s ~60–90° period. There was a north polar data gap at $L_s \sim 70°$, but the final orbits of Cassini around northern summer solstice ($L_s = 90°$) showed that north polar gases had attained almost equatorial abundances and vortex breakup was complete.

Interestingly, our results show that after vortex breakup, spreading of air enriched in trace gases to lower latitudes did not occur (Figure 3). This shows that polar gas depletion by small-scale cross-latitude mixing, which would enhance trace gas abundances at subpolar latitudes postvortex breakup, is small compared to other effects. Furthermore, this suggests that the bulk of stratospheric trace gas loss must be due to a combination of large-scale dynamics and photochemistry. In this scenario, upwelling from the reversed meridional Hadley circulation would advect trace gas depleted air from lower latitudes into the north polar midstratosphere, leading to a reduction in abundances. Photochemical loss, enabled by increasing insolation after

equinox, could also contribute to a reduction in polar stratospheric trace gas abundance during northern spring.

4.3. South Polar Vortex Evolution

South polar nadir observations have a data gap after equinox, but previous limb viewing observations showed the south polar winter vortex formed almost immediately after northern spring equinox (Teanby et al., 2012; Vinatier et al., 2015). Early southern winter vortex temperatures dramatically cooled to ~120 K during L_s = 0–60° at 1 mbar. This is much colder than was observed in the middle-winter north polar vortex and can explain the high-altitude HCN and C_6H_6 ice clouds observed by de Kok et al. (2014) and Vinatier et al. (2018). The extremely cold temperatures could be caused by enhanced radiative cooling from enriched trace gases, which are effective infrared coolers (Bézard et al., 2018; Teanby et al., 2017). In the early stages of vortex formation this cooling was not mitigated by significant adiabatic heating as the reversed meridional Hadley circulation was initially quite sluggish (Teanby et al., 2012, 2017). It is also possible that enhancement of infrared cooling gases may form a radiative feedback, contributing to establishing the reversed circulation (Teanby et al., 2017). Postequinox the south polar vortex continued to grow and by $L_s \sim 90°$ it was similar in extent to the middle-winter northern vortex, reaching 45°S. It is likely that the early northern winter vortex also exhibited this behavior, but this phase would occur for L_s = 180–270° prior to Cassini's arrival, so remains unobserved.

For the shortest-lifetime gases (e.g., HC_3N and C_4H_2), there appeared to be some overshoot of enrichment during vortex formation, with south polar abundances being enhanced by up to an order of magnitude compared to those observed in the middle-winter north polar vortex. This can be seen in Figure 4, with abundances peaking around L_s = 60–90° at 80°S. Therefore, the largest winter polar trace gas enrichments occurred between equinox and winter solstice. This effect was also visible in limb observations (Teanby et al., 2012, 2017; Vinatier et al., 2015), but with peak abundances occurring earlier ($L_s < 60°$) at high altitude (>300 km, <0.1 mbar) and later ($L_s > 60°$) at low altitude (<300 km, >0.1 mbar). Near the end of the mission (L_s = 93°), temperatures and abundances appeared to be trending toward those observed in northern midwinter (Figure 4). This suggests that north and south polar vortices have similar temperatures and chemistry at similar seasonal phases.

One potential explanation for the extreme south polar enrichments observed during L_s = 0–90° requires a combination of photochemistry, insolation, and dynamics. Close to equinox, upper atmosphere abundances of trace gases were highest because the southern hemisphere was just exiting summer—a period of relatively high insolation and photochemical production. Then, after equinox, as the circulation reversed and subsidence developed, the trace gas vertical profiles were advected downward, leading to large stratospheric enrichments. However, as the season progressed, overall insolation in the southern hemisphere steadily decreased, in turn reducing upper atmosphere photochemical production, which led to lower trace gas abundances at high altitude. This reduced the supply of trace gases into the vortex and led to less extreme polar enrichments. The latitude extent of the vortex also could play a role. Initially, the vortex had a small-latitude extent, so drew air from the upper atmosphere directly above the pole, which had constant illumination above 300-km altitude throughout winter, but as the vortex grew the air in the vortex was sourced from a wider region of the southern hemisphere, which had lower insolation and reduced upper atmosphere trace gas abundances. This conceptual explanation would need a coupled GCM and photochemical model to investigate further.

4.4. Equatorial Temperatures

The 1 mbar temperature maximum was skewed toward the subsolar point but stayed within 10° of the equator. The temperature at 5 mbar exhibited a steady 5-K cooling from L_s = 293–93°, which was caused by the increase in Sun-Saturn distance over the mission (Figure 1a). This effect was also clearly observed in the lower stratosphere (10–30 mbar) in previous analysis of far-infrared FP1 spectra (Sylvestre et al., 2019). At lower pressures (~1–0.1 mbar) dynamics had a larger effect on the temperature (Bézard et al., 2018) and the effect of the increasing Sun-Saturn distance was less apparent.

5. Conclusions

Cassini CIRS nadir mapping observations of Titan were analyzed for the entire mission duration, which ran from northern midwinter (L_s = 293°) until just after northern summer solstice (L_s = 93°), to obtain seasonal

latitude variation maps at the 1-mbar pressure level. The equatorial composition was stable for all the species analyzed, whereas the midlatitudes and polar regions exhibited significant variability.

Winter vortices were observed at both poles with cold temperatures and isolated air masses enriched in trace gas species. The enrichments were largest for short-lifetime gases and more modest for those with longer lifetimes, in keeping with previous studies (Teanby et al., 2009, 2010a). However, early- and middle-winter vortices evidently had very different properties. When newly formed, the south polar vortex was significantly more enriched in trace gases and achieved colder temperatures than its established northern counterpart. Trace gas abundances were up to an order of magnitude greater at the southern early-winter pole than the northern middle-winter pole. This could be due to enhanced radiative cooling from trace gases combined with a relatively weak subsidence and initially steeper photochemical profiles during vortex formation. This suggests early vortex temperature structure was dominated by radiative cooling, whereas middle-winter vortex temperatures were dominated by subsidence-driven adiabatic heating.

Dissipation of the north polar vortex was a gradual process and was only complete ~90° of L_s after equinox. Gas enrichments did not appear to spread from high to low latitudes during vortex breakup, suggesting that photochemistry and depletion due to large-scale dynamics related to the meridional circulation (upwelling) were more important loss mechanisms than small-scale cross-latitude mixing. Near the end of the mission the temperature and composition of the south polar vortex were trending toward those observed in the north at the start of the mission. However, as the Cassini data set covers $\Delta L_s = 160°$, we are 20° of L_s short of a complete half Titan year record. Therefore, it is not possible to definitively confirm that north and south poles reach equivalent states for equivalent seasons, although a short extrapolation of the data suggests seasonal equivalence is very likely. This implies temperature and composition differences between the middle-winter north polar vortex and early-winter south polar vortex were primarily due to seasonal phase, not any hemispheric asymmetry.

Over the next few years it will be important to observe the north polar temperature and composition using ground- and space-based facilities such as ALMA and JWST. ALMA has already produced moderate resolution latitude maps, which have the potential to complete the CIRS record at high northern latitudes (Thelen et al., 2019, 2018). Unfortunately, with the loss of Cassini, the winter poles can no longer be observed until we next visit Titan.

Acknowledgments
N. A. T., M. S., J. S., and P. G. J. I. were funded by the UK Science and Technology Facilities Council (STFC). C. A. N. was supported by the NASA Cassini project and the NASA Astrobiology Institute. S. V. was funded by the French Centre National d'Etudes Spatiales (CNRS). The Cassini CIRS observations, summarized in Table S1, are publicly available from NASA's Planetary Data System (https://pds.nasa.gov). Temperature and composition results from this paper are available in supporting Data Sets S1 and S2, with a gridded NetCDF format product in Data set S3.

References

Achterberg, R. K., Conrath, B. J., Gierasch, P. J., Flasar, F. M., & Nixon, C. A. (2008). Titan's middle-atmospheric temperatures and dynamics observed by the Cassini Composite Infrared Spectrometer. *Icarus*, *194*, 263–277.

Achterberg, R. K., Gierasch, P. J., Conrath, B. J., Flasar, F. M., & Nixon, C. A. (2011). Temporal variations of Titan's middle-atmospheric temperatures from 2004 to 2009 observed by Cassini/CIRS. *Icarus*, *211*, 686–698.

Bézard, B. (2014). The composition of Titan's atmosphere. In I. Müller-Wodarg, C. A. Griffith, E. Lellouch, & T. E. Cravens (Eds.), *Titan: Interior, surface, atmosphere, and space environment* (pp. 158–189). Cambridge: Cambridge University Press.

Bézard, B., Coustenis, A., & McKay, C. P. (1995). Titan's stratospheric temperature asymmetry—A radiative origin. *Icarus*, *113*, 267–276.

Bézard, B., Vinatier, S., & Achterberg, R. K. (2018). Seasonal radiative modeling of Titan's stratospheric temperatures at low latitudes. *Icarus*, *302*, 437–450.

Borysow, A., & Frommhold, L. (1987). Collision-induced rototranslational absorption spectra of CH_4-CH_4 pairs at temperatures from 50 to 300 K. *The Astrophysical Journal*, *318*, 940–943.

Coustenis, A., Achterberg, R. K., Conrath, B. J., Jennings, D. E., Marten, A., Gautier, D., et al. (2007). The composition of Titan's stratosphere from Cassini/CIRS mid-infrared spectra. *Icarus*, *189*, 35–62.

Coustenis, A., & Bézard, B. (1995). Titan's atmosphere from Voyager infrared observations. IV. Spatial variations of temperature and composition. *Icarus*, *115*, 126–140.

Coustenis, A., Bézard, B., Gautier, D., Marten, A., & Samuelson, R. (1991). Titan's atmosphere from Voyager infrared observations. III. Vertical distributions of hydrocarbons and nitriles near Titan's north-pole. *Icarus*, *89*, 152–167.

Coustenis, A., Jennings, D. E., Achterberg, R. K., Bampasidis, G., Lavvas, P., Nixon, C. A., et al. (2016). Titan's temporal evolution in stratospheric trace gases near the poles. *Icarus*, *270*, 409–420.

Coustenis, A., Jennings, D. E., Achterberg, R. K., Bampasidis, G., Nixon, C. A., Lavvas, P., et al. (2018). Seasonal evolution of Titan's stratosphere near the poles. *The Astrophysical Journal*, *854*, L30. https://doi.org/10.3847/2041-8213/aaadbd

Coustenis, A., Nixon, C. A., Achterberg, R. K., Lavvas, P., Vinatier, S., Teanby, N. A., et al. (2010). Titan trace gaseous composition from CIRS at the end of the Cassini-Huygens prime mission. *Icarus*, *207*, 461–476.

de Kok, R., Irwin, P. G. J., Teanby, N. A., Vinatier, S., Negrão, A., Osprey, S., et al. (2010). A tropical haze band in Titan's stratosphere. *Icarus*, *207*, 485–490.

de Kok, R. J., Teanby, N. A., Maltagliati, L., Irwin, P. G. J., & Vinatier, S. (2014). HCN ice in Titan's high-altitude southern polar cloud. *Nature*, *514*, 65–67.

Dobrijevic, M., Hébrard, E., Loison, J. C., & Hickson, K. M. (2014). Coupling of oxygen, nitrogen, and hydrocarbon species in the photochemistry of Titan's atmosphere. *Icarus*, *228*, 324–346.

Flasar, F. M., Achterberg, R. K., Conrath, B. J., Gierasch, P. J., Kunde, V. G., Nixon, C. A., et al. (2005). Titan's atmospheric temperatures, winds, and composition. *Science*, *308*, 975–978.

Flasar, F. M., Kunde, V. G., Abbas, M. M., Achterberg, R. K., Ade, P., Barucci, A., et al. (2004). Exploring the Saturn system in the thermal infrared: The Composite Infrared Spectrometer. *Space Science Reviews*, *115*, 169–297.

Fulchignoni, M., Ferri, F., Angrilli, F., Ball, A. J., Bar-Nun, A., Barucci, M. A., et al. (2005). In situ measurements of the physical characteristics of Titan's environment. *Nature*, *438*, 785–791.

Hörst, S. M., Vuitton, V., & Yelle, R. V. (2008). Origin of oxygen species in Titan's atmosphere. *Journal of Geophysical Research*, *113*, E10006. https://doi.org/10.1029/2008JE003135

Hourdin, F., Talagrand, O., Sadourny, R., Courtin, R., Gautier, D., & McKay, C. P. (1995). Numerical simulation of the general circulation of the atmosphere of Titan. *Icarus*, *117*, 358–374.

Irwin, P. G. J., Teanby, N. A., de Kok, R., Fletcher, L. N., Howett, C. J. A., Tsang, C. C. C., et al. (2008). The NEMESIS planetary atmosphere radiative transfer and retrieval tool. *Journal of Quantitative Spectroscopy and Radiative Transfer*, *109*, 1136–1150.

Krasnopolsky, V. A. (2009). A photochemical model of Titan's atmosphere and ionosphere. *Icarus*, *201*, 226–256.

Lavvas, P. P., Coustenis, A., & Vardavas, I. M. (2008). Coupling photochemistry with haze formation in Titan's atmosphere, Part II: Results and validation with Cassini/Huygens data. *Planetary & Space Science*, *56*, 67–99.

Le Mouélic, S., Rodriguez, S., Robidel, R., Rousseau, B., Seignovert, B., Sotin, C., et al. (2018). Mapping polar atmospheric features on Titan with VIMS: From the dissipation of the northern cloud to the onset of a southern polar vortex. *Icarus*, *311*, 371–383. https://doi.org/10.1016/j.icarus.2018.04.028

Lebonnois, S., Burgalat, J., Rannou, P., & Charnay, B. (2012). Titan global climate model: A new 3-dimensional version of the IPSL Titan GCM. *Icarus*, *218*, 707–722.

Lebonnois, S., Flasar, F. M., Tokano, T., & Newman, C. E. (2014). The general circulation of Titan's lower and middle atmosphere. In *Titan: Interior, surface, atmosphere, and space environment* (pp. 122–157).

Loison, J. C., Hébrard, E., Dobrijevic, M., Hickson, K. M., Caralp, F., Hue, V., et al. (2015). The neutral photochemistry of nitriles, amines and imines in the atmosphere of Titan. *Icarus*, *247*, 218–247.

Lora, J. M., Lunine, J. I., & Russell, J. L. (2015). GCM simulations of Titan's middle and lower atmosphere and comparison to observations. *Icarus*, *250*, 516–528. https://doi.org/10.1016/j.icarus.2014.12.030

Newman, C. E., Lee, C., Lian, Y., Richardson, M. I., & Toigo, A. D. (2011). Stratospheric superrotation in the TitanWRF model. *Icarus*, *213*, 636–654.

Smith, W. H. F., & Wessel, P. (1990). Gridding with continuous curvature splines in tension. *Geophysics*, *55*, 293–305.

Sylvestre, M., Teanby, N. A., Vinatier, S., Lebonnois, S., & Irwin, P. G. J. (2018). Seasonal evolution of C_2N_2, C_3H_4, and C_4H_2 abundances in Titan's lower stratosphere. *Astronomy & Astrophysics*, *609*(A64), 13. https://doi.org/10.1051/0004-6361/201630255

Sylvestre, M., Teanby, N. A., Vinatier, S., Lebonnois, S., & Irwin, P. G. J. (2019). Seasonal evolution of temperatures in Titan's lower stratosphere. *Icarus*. https://doi.org/10.1016/j.icarus.2019.02.003

Teanby, N. A. (2007). Constrained smoothing of noisy data using splines in tension. *Mathematical Geology*, *39*, 419–434.

Teanby, N. A., Bézard, B., Vinatier, S., Sylvestre, M., Nixon, C. A., Irwin, P. G. J., et al. (2017). The formation and evolution of Titan's winter polar vortex. *Nature Communications*, *8*(1), 1586.

Teanby, N. A., de Kok, R., Irwin, P. G. J., Osprey, S., Vinatier, S., Gierasch, P. J., et al. (2008). Titan's winter polar vortex structure revealed by chemical tracers. *Journal of Geophysical Research*, *113*, E12003. https://doi.org/10.1029/2008JE003218

Teanby, N. A., Irwin, P. G. J., de Kok, R., & Nixon, C. A. (2009). Dynamical implications of seasonal and spatial variations in Titan's stratospheric composition. *Philosophical Transactions of the Royal Society of London. Series A*, *367*, 697–711.

Teanby, N. A., Irwin, P. G. J., de Kok, R., & Nixon, C. A. (2010a). Mapping Titan's HCN in the far infra-red: Implications for photochemistry. *Faraday Discussions*, *147*, 51–64.

Teanby, N. A., Irwin, P. G. J., de Kok, R., & Nixon, C. A. (2010b). Seasonal changes in Titan's polar trace gas abundance observed by Cassini. *The Astrophysical Journal*, *724*, L84–L89.

Teanby, N. A., Irwin, P. G. J., de Kok, R., Nixon, C. A., Coustenis, A., Bézard, B., et al. (2006). Latitudinal variations of HCN, HC_3N, and C_2N_2 in Titan's stratosphere derived from Cassini CIRS data. *Icarus*, *181*, 243–255.

Teanby, N. A., Irwin, P. G. J., de Kok, R., Nixon, C. A., Coustenis, A., Royer, E., et al. (2008). Global and temporal variations in hydrocarbons and nitriles in Titan's stratosphere for northern winter observed by Cassini/CIRS. *Icarus*, *193*, 595–611.

Teanby, N. A., Irwin, P. G. J., de Kok, R., Vinatier, S., Bézard, B., Nixon, C. A., et al. (2007). Vertical profiles of HCN, HC_3N, and C_2H_2 in Titan's atmosphere derived from Cassini/CIRS data. *Icarus*, *186*, 364–384.

Teanby, N. A., Irwin, P. G. J., Nixon, C. A., de Kok, R., Vinatier, S., Coustenis, A., et al. (2012). Active upper-atmosphere chemistry and dynamics from polar circulation reversal on Titan. *Nature*, *491*, 732–735. https://doi.org/10.1038/nature11611

Thelen, A. E., Nixon, C. A., Chanover, N. J., Cordiner, M. A., Molter, E. M., Teanby, N. A., et al. (2019). Abundance measurements of Titan's stratospheric HCN, HC_3N, C_3H_4, and CH_3CN from ALMA observations. *Icarus*, *319*, 417–432. https://doi.org/10.1016/j.icarus.2018.09.023

Thelen, A. E., Nixon, C. A., Chanover, N. J., Molter, E. M., Cordiner, M. A., Achterberg, R. K., et al. (2018). Spatial variations in Titan's atmospheric temperature: ALMA and Cassini comparisons from 2012 to 2015. *Icarus*, *307*, 380–390. https://doi.org/10.1016/j.icarus.2017.10.042

Vinatier, S., Bézard, B., de Kok, R., Anderson, C. M., Samuelson, R. E., Nixon, C. A., et al. (2010). Analysis of Cassini/CIRS limb spectra of Titan acquired during the nominal mission. II: aerosol extinction profiles in the 600–1420 cm^{-1} spectral range. *Icarus*, *210*, 852–866.

Vinatier, S., Bézard, B., Fouchet, T., Teanby, N. A., de Kok, R., Irwin, P. G. J., et al. (2007). Vertical abundance profiles of hydrocarbons in Titan's atmosphere at 15°S and 80°N retrieved from Cassini/CIRS spectra. *Icarus*, *188*, 120–138.

Vinatier, S., Bézard, B., Lebonnois, S., Teanby, N. A., Achterberg, R. K., Gorius, N., et al. (2015). Seasonal variations in Titan's middle atmosphere during the northern spring derived from Cassini/CIRS observations. *Icarus*, *250*, 95–115.

Vinatier, S., Bézard, B., Nixon, C. A., Mamoutkine, A., Carlson, R. C., Jennings, D. E., et al. (2010). Analysis of Cassini/CIRS limb spectra of Titan acquired during the nominal mission I. Hydrocarbons, nitriles and CO_2 vertical mixing ratio profiles. *Icarus*, *205*, 559–570.

Vinatier, S., Schmitt, B., Bézard, B., Rannou, P., Dauphin, C., de Kok, R., et al. (2018). Study of Titan's fall southern stratospheric polar cloud composition with Cassini/CIRS: Detection of benzene ice. *Icarus*, *310*, 89–104. https://doi.org/10.1016/j.icarus.2017.12.040

Vuitton, V., Yelle, R. V., Klippenstein, S. J., Hörst, S. M., & Lavvas, P. (2019). Simulating the density of organic species in the atmosphere of Titan with a coupled ion-neutral photochemical model. *Icarus*, *324*, 120–197.

West, R. A., Seignovert, B., Rannou, P., Dumont, P., Turtle, E. P., Perry, J., et al. (2018). The seasonal cycle of Titan's detached haze. *Nature Astronomy*, *2*, 495–500. https://doi.org/10.1038/s41550-018-0434-z

Wilson, E. H., & Atreya, S. K. (2004). Current state of modeling the photochemistry of Titan's mutually dependent atmosphere and ionosphere. *Journal of Geophysical Research*, *109*, E06002. https://doi.org/10.1029/2003JE002181

References from Supporting Information

Borysow, A. (1991). Modelling of collision-induced infrared-absorption spectra of H_2-H_2 pairs in the fundamental band at temperatures from 20 K to 300 K. *Icarus*, *92*(2), 273–279.

Borysow, A., & Frommhold, L. (1986a). Collision-induced rototranslational absorption spectra of N_2-N_2 pairs for temperatures from 50 to 300 K. *The Astrophysical Journal*, *311*, 1043–1057.

Borysow, A., & Frommhold, L. (1986b). Theoretical collision-induced rototranslational absorption spectra for modeling Titan's atmosphere: H_2-N_2 pairs. *The Astrophysical Journal*, *303*, 495–510.

Borysow, A., & Frommhold, L. (1986c). Theoretical collision-induced rototranslational absorption spectra for the outer planets: H_2-CH_4 pairs. *The Astrophysical Journal*, *304*, 849–865.

Borysow, A., & Tang, C. (1993). Far infrared CIA spectra of N_2-CH_4 pairs for modeling of Titan's atmosphere. *Icarus*, *105*, 175–183.

de Kok, R., Irwin, P. G. J., Teanby, N. A., Lellouch, E., Bezard, B., Vinatier, S., et al. (2007a). Oxygen compounds in Titan's stratosphere as observed by Cassini CIRS. *Icarus*, *186*, 354–363.

de Kok, R., Irwin, P. G. J., Teanby, N. A., Nixon, C. A., Jennings, D. E., Fletcher, L., et al. (2007b). Characteristics of Titan's stratospheric aerosols and condensate clouds from Cassini CIRS far-infrared spectra. *Icarus*, *191*, 223–235.

Haynes, W. M. (Ed.) (2011). *CRC handbook of chemistry and physics* (92nd ed.). Bosa Roca: Taylor & Francis Inc.

Jacquinet-Husson, N., Armante, R., Scott, N. A., Chédin, A., Crépeau, L., Boutammine, C., et al. (2016). The 2015 edition of the GEISA spectroscopic database. *Journal of Molecular Spectroscopy*, *327*, 31–72.

Jennings, D. E., Flasar, F. M., Kunde, V. G., Nixon, C. A., Segura, M. E., Romani, P. N., et al. (2017). Composite infrared spectrometer (CIRS) on Cassini. *Applied Optics*, *56*, 5274. https://doi.org/10.1364/ao.56.005274

Kunde, V., Ade, P., Barney, R., Bergman, D., Bonnal, J. F., Borelli, R., et al. (1996). Cassini infrared Fourier spectroscopic investigation. *Proc Soc Photo-Opt Instrum Eng*, *2803*, 162–177.

Niemann, H. B., Atreya, S. K., Demick, J. E., Gautier, D., Haberman, J. A., Harpold, D. N., et al. (2010). Composition of Titan's lower atmosphere and simple surface volatiles as measured by the Cassini-Huygens probe gas chromatograph mass spectrometer experiment. *Journal of Geophysical Research*, *115*, E12006. https://doi.org/10.1029/2010JE003659

Nixon, C. A., Teanby, N. A., Calcutt, S. B., Aslam, S., Jennings, D. E., Kunde, V. G., et al. (2009). Infrared limb sounding of Titan with the Cassini Composite Infrared Spectrometer: Effects of the mid-IR detector spatial responses. *Applied Optics*, *48*, 1912–1925.

Rothman, L. S., Gordon, I. E., Babikov, Y., Barbe, A., Benner, D. C., Bernath, P. F., et al. (2013). The HITRAN2012 molecular spectroscopic database. *Journal of Quantitative Spectroscopy and Radiation Transfer*, *130*, 4–50.

Tomasko, M. G., Doose, L., Engel, S., Dafoe, L. E., West, R., Lemmon, M., et al. (2008). A model of Titan's aerosols based on measurements made inside the atmosphere. *Planetary & Space Science*, *56*, 669–707.

Vinatier, S., Rannou, P., Anderson, C. M., Bézard, B., de Kok, R., & Samuelson, R. E. (2012). Optical constants of Titan's stratospheric aerosols in the 70–1500 cm^{-1} spectral range constrained by Cassini/CIRS observations. *Icarus*, *219*, 5–12.